# Supplementary information

# Solar-Complemented Moisture Electric Generator for Synergistic Energy Harvesting in All Regions

Gangli Zhao [a, b, c, #], Daozhi Shen [a, b, #, *], Shuaiqi Han [a], Dingyun Zhang [a], Linglan Guo [a], Qiaolin Gu [a], Feng Zhan [c], Limin Zhu [d, *]

[a] *State Key Laboratory of Micro-nano Engineering Science, School of Mechanical Engineering，Shanghai Jiao Tong University, Shanghai 200240, China*

[b] *National Center for Translational Medicine, Shanghai Jiao Tong University, Shanghai 200240, China*

[c] *School of Resources, Environment and Materials, Guangxi University, Nanning 530004, China*

[d] *State Key Laboratory of Mechanical System and Vibration, School of Mechanical Engineering, Shanghai Jiao Tong University, Shanghai, 200240, China*

[#] *These authors contribute equally.*

**Email: dzshen@sjtu.edu.cn; zhulm@sjtu.edu.cn*

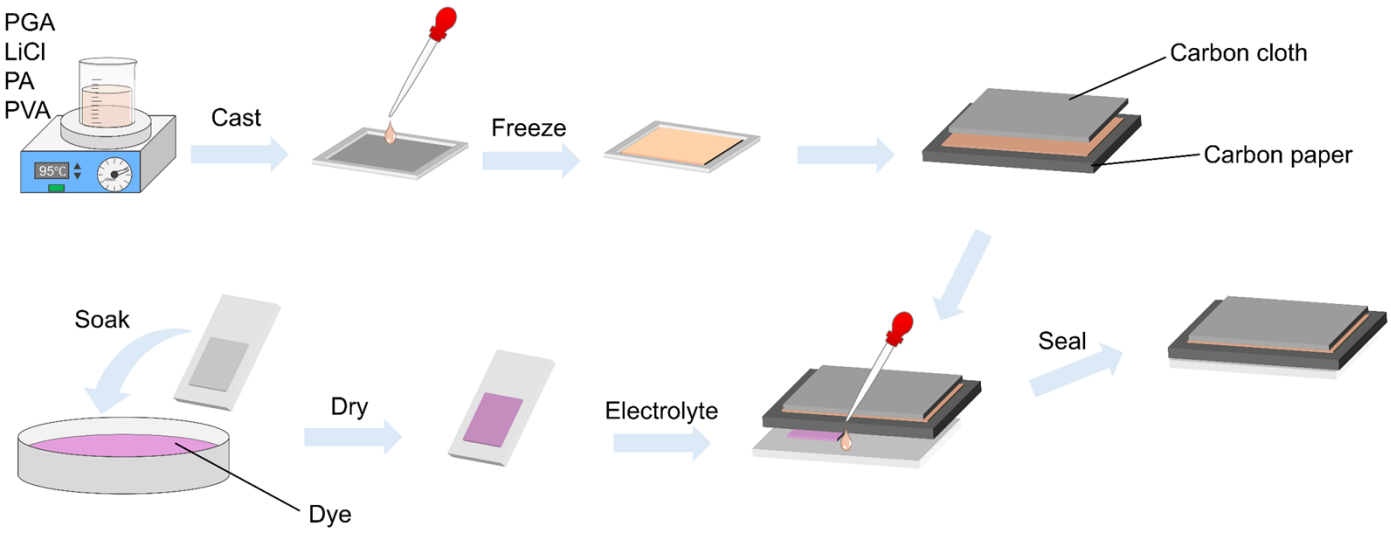


**Fig. S1** Schematic illustration of the step-by-step fabrication process of the MEG–SC hybrid generator.

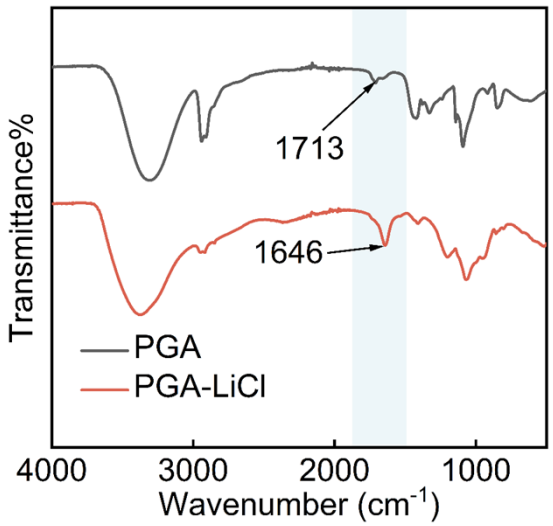


**Fig. S2** Transmission FTIR spectra of PGA and PGA–LiCl.

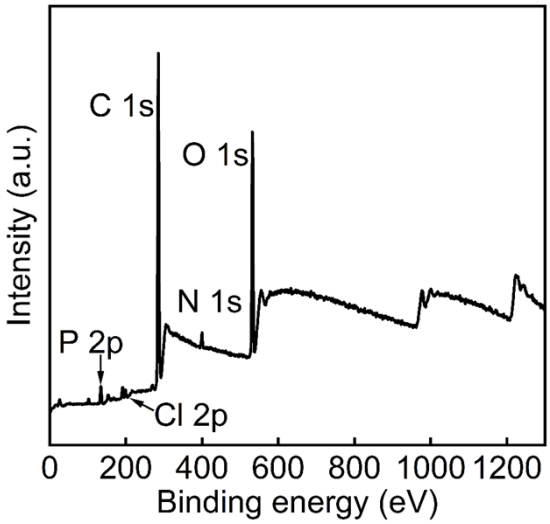


**Fig. S3** XPS spectra of PGA-LiCl-PA-PVA.

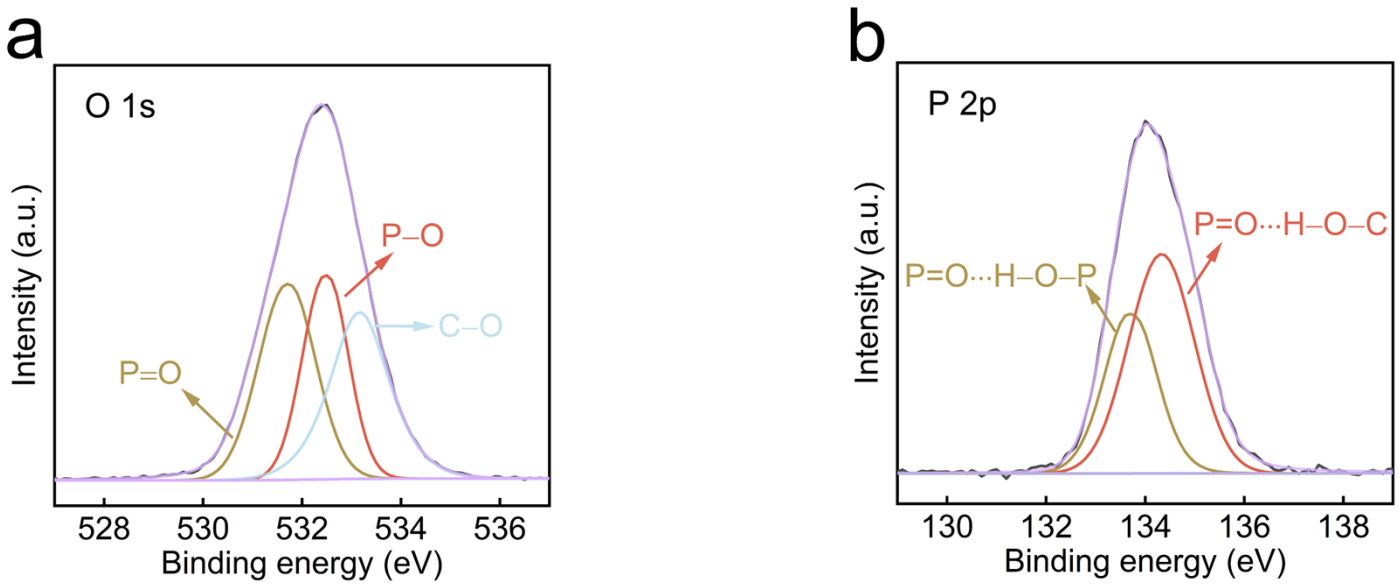


**Fig. S4** XPS survey spectrum of the ionic hydrogel and the corresponding high-resolution spectra of (a) O 1s and (b) P 2p.

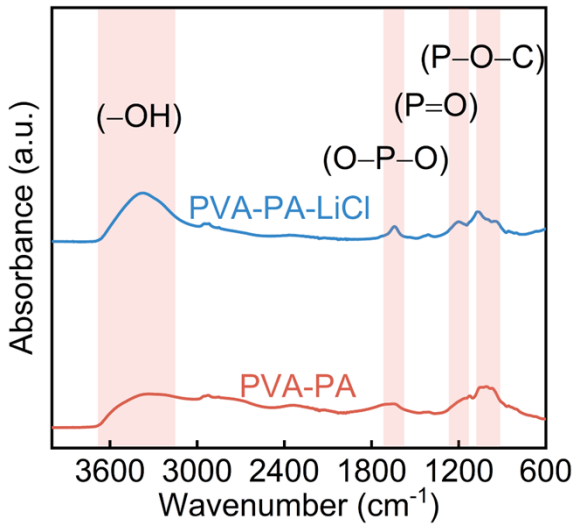


**Fig. S5** FTIR absorption spectra of PVA–PA–LiCl and PVA–PA.

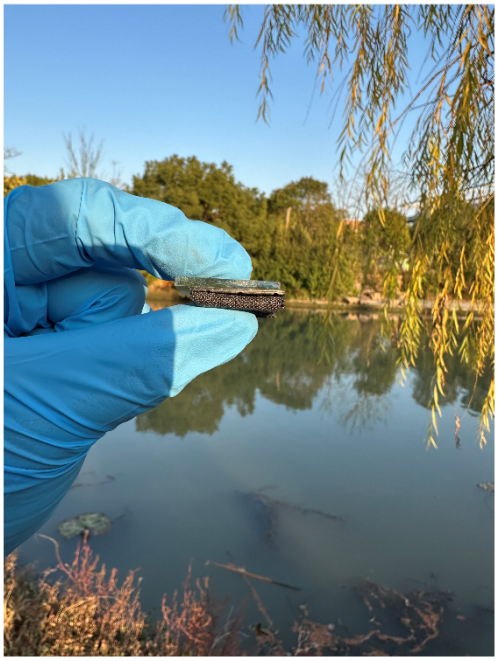

**Fig. S6** Optical microscopy image of the MEG–SC hybrid generator.

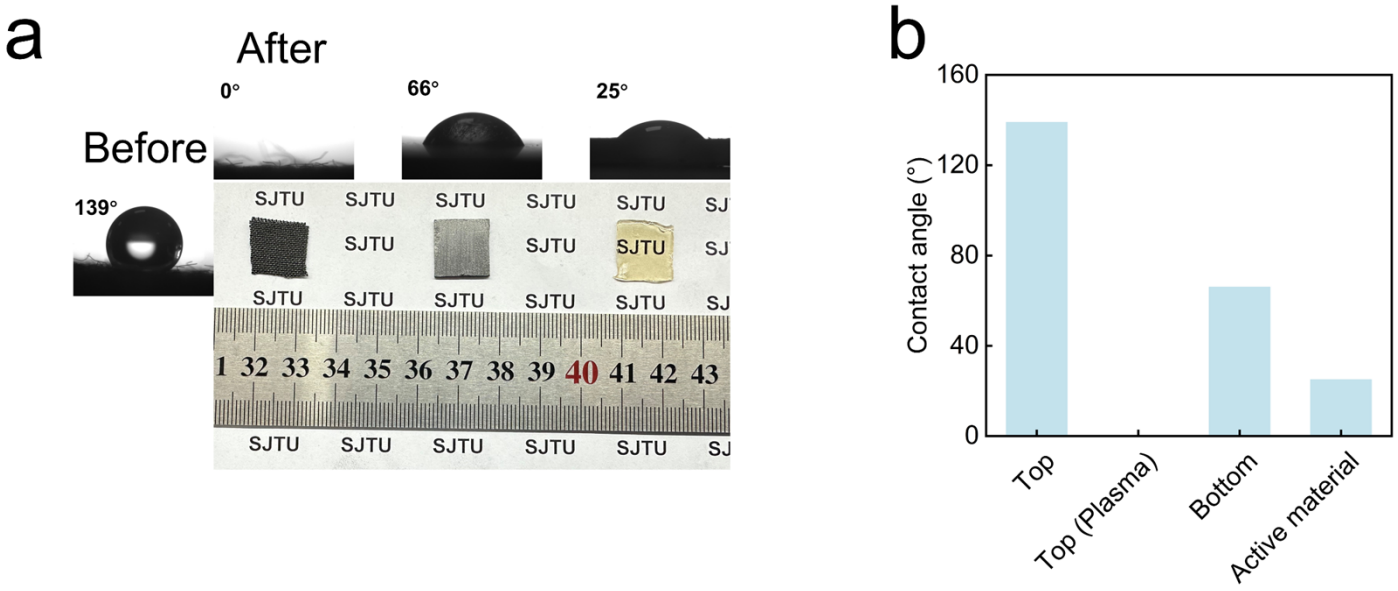


**Fig. S7** Photographs and water contact angle measurements of the MEG components. (a) Top electrode before plasma treatment, top electrode after plasma treatment, bottom electrode, and active layer (from left to right) (b) Statistical data chart.

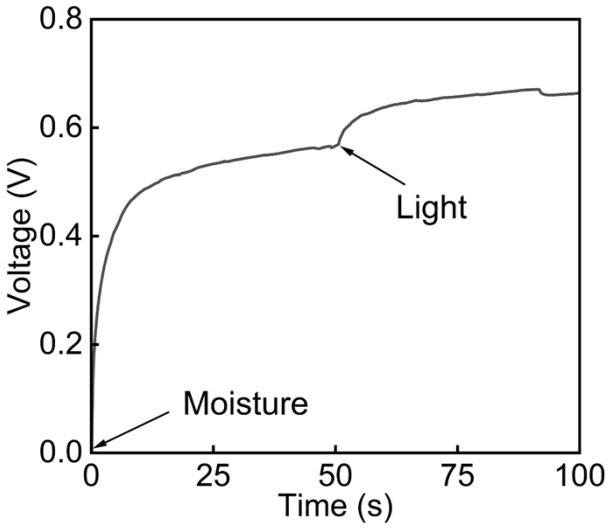


**Fig. S8** Voc output of the MEG–SC hybrid generator.

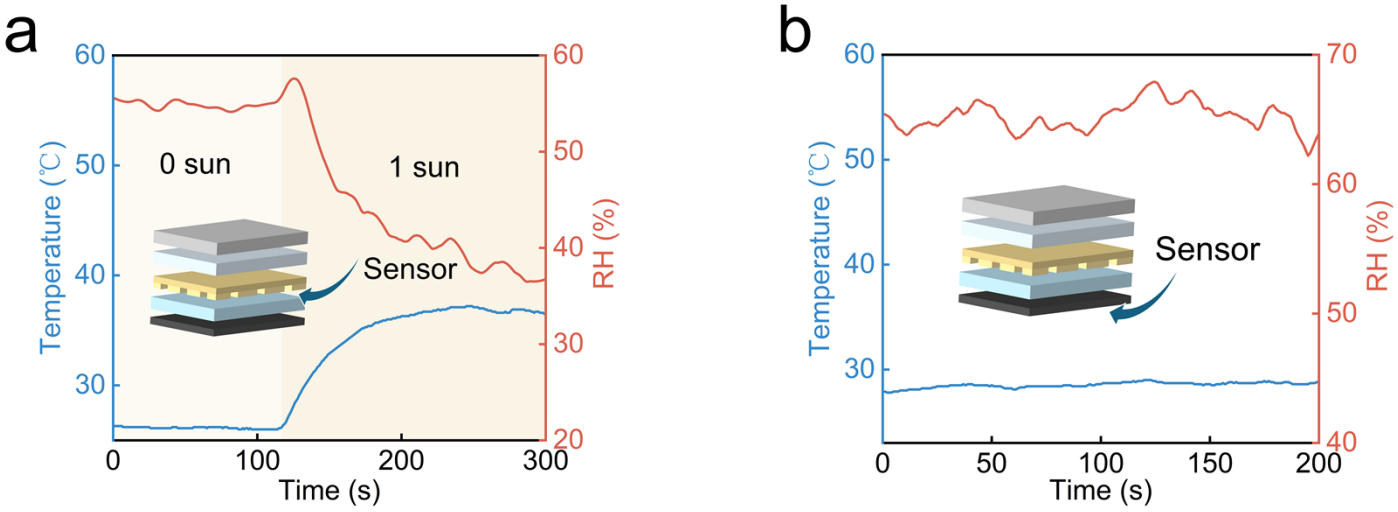


**Fig. S9** Humidity and temperature records of the MEG–SC hybrid generator under 1 Sun illumination: (a) evaporation side of the MEG and (b) hygroscopic side of the MEG.

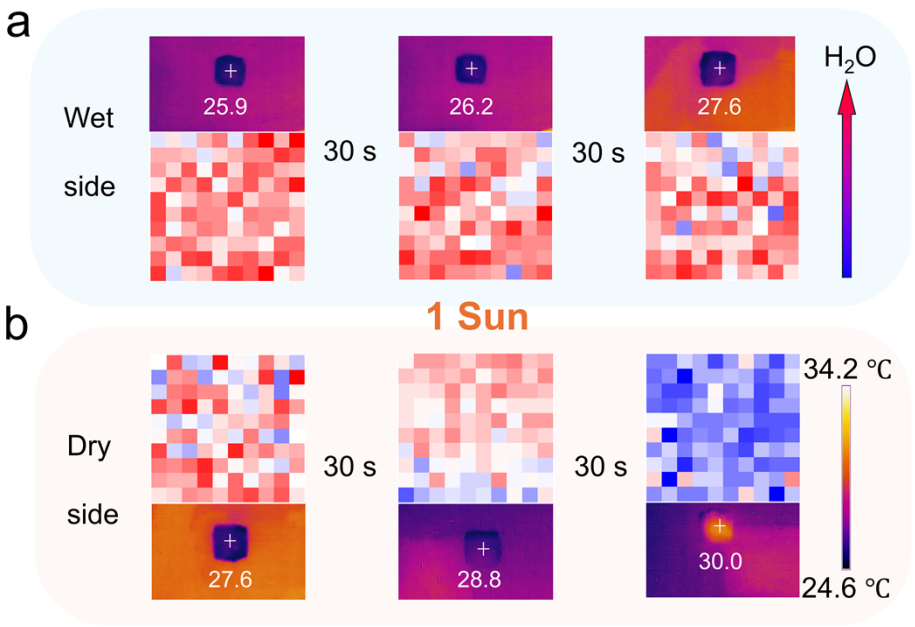


**Fig. S10** Infrared images and Raman mapping of the surface water content on the wet side (a) and dry side (b) of the hydrogel at 30 s intervals under 1 sun illumination.

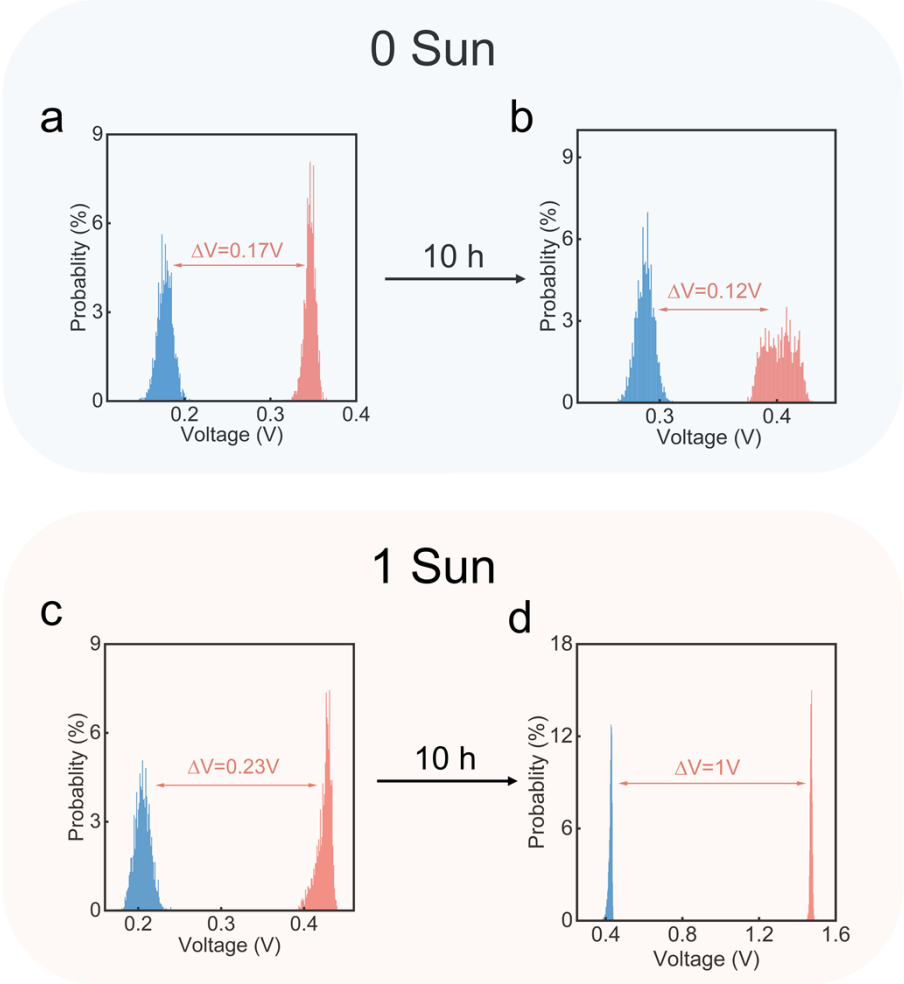


**Fig. S11** KPFM characterization of the potential difference between the two sides of the PLPP hydrogel under different illumination conditions: (a) without illumination, (b) without illumination after 10 h, (c) under 1 Sun illumination, and (d) under 1 Sun illumination after 10 h.

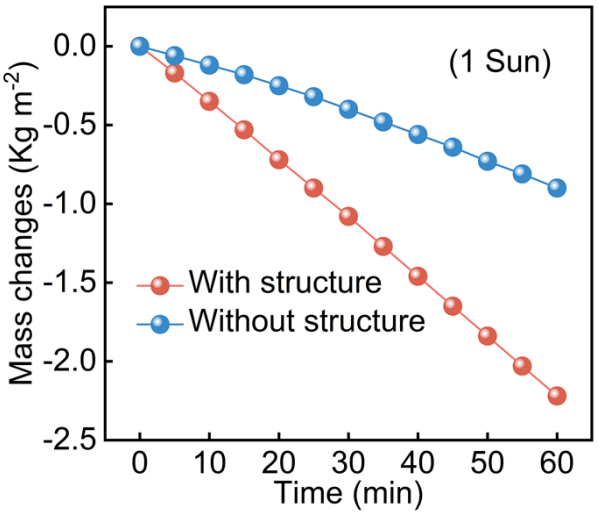


**Fig. S12** Mass change of the hydrogel with and without the evaporation structure.

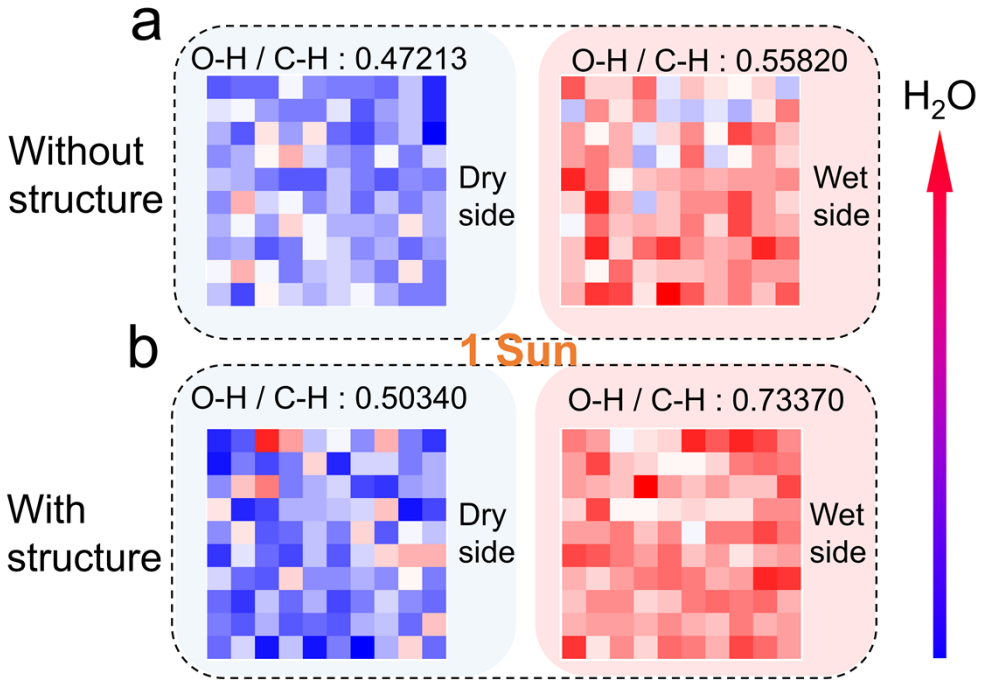


**Fig. S13** Raman mapping images of surface water content and the corresponding average O–H/C–H intensity ratios on the dry and wet sides of the PLPP hydrogel under 1 sun illumination: (a) without structural design and (b) with structural design.

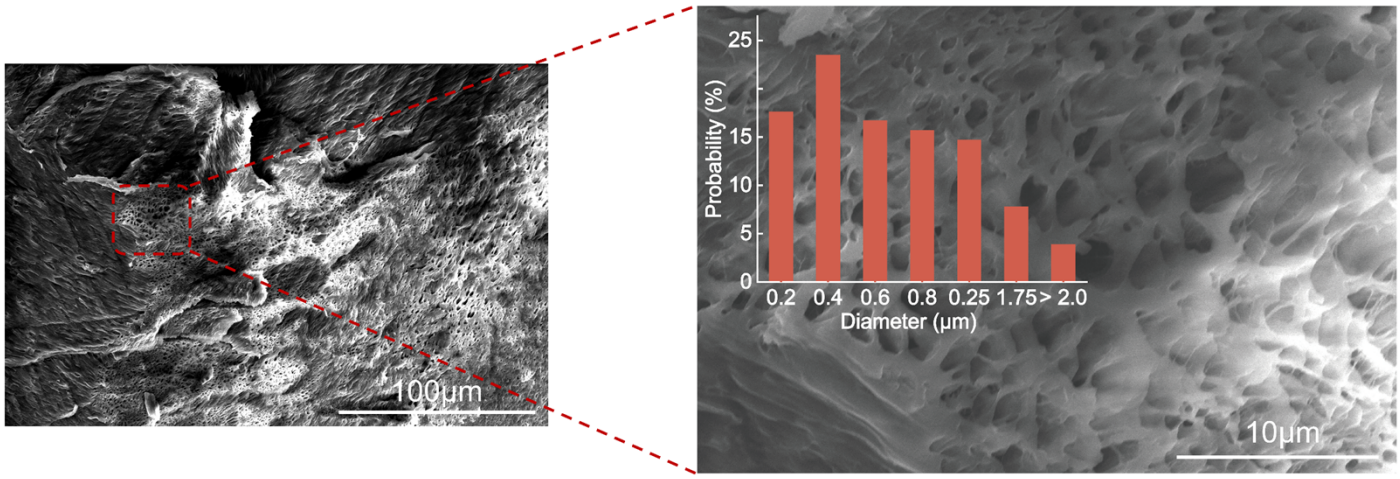


**Fig. S14** SEM images of the PGA-LiCl-PA hydrogel at different magnifications.

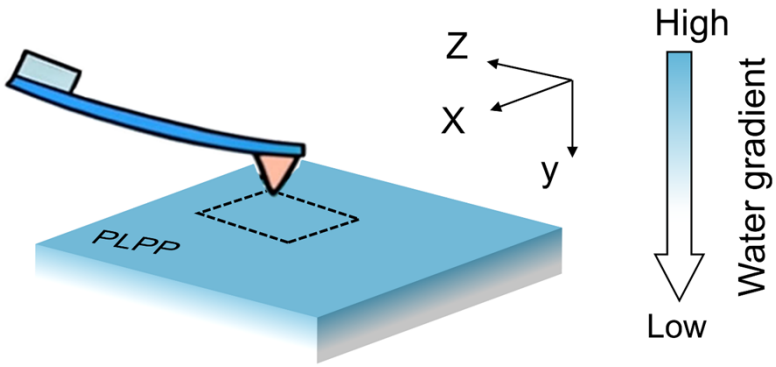


**Fig. S15** Schematic illustration of the KPFM characterization.

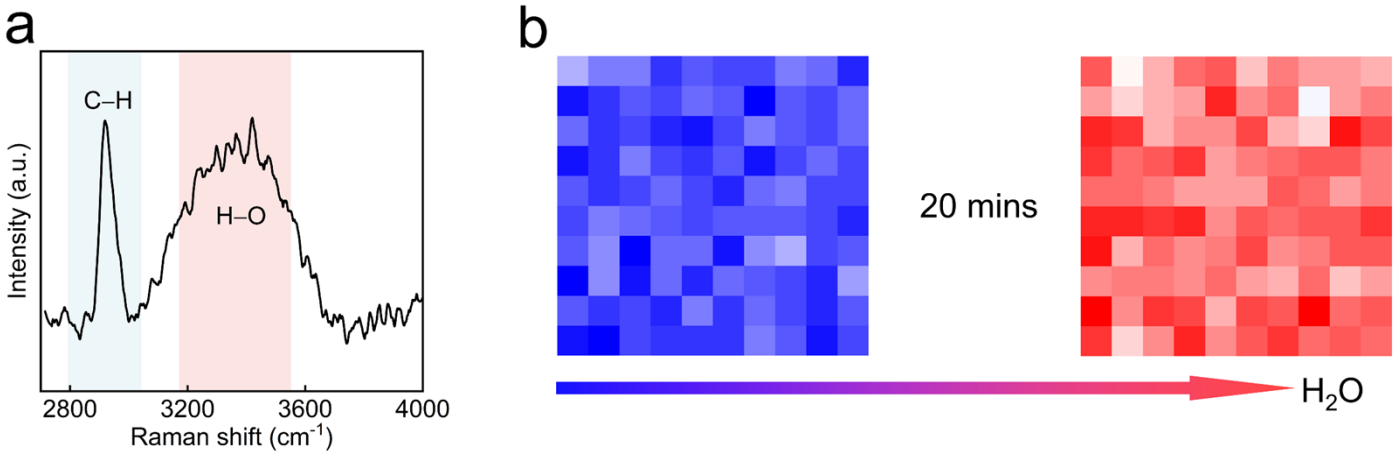


**Fig. S16** Raman characterization of PLPP hydrogel. (a) Raman spectra of the surface of the PLPP hydrogel. (b) Water absorption behavior of the PLPP hydrogel under a humid environment at RH 60%.

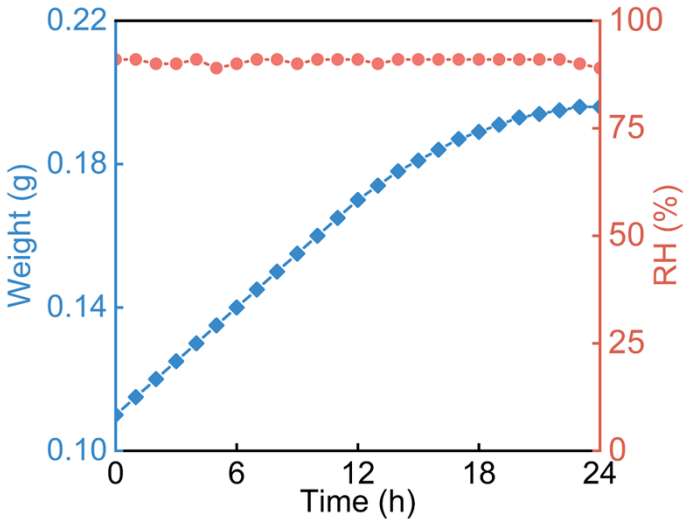


**Fig. S17** Moisture absorption of the PLPP hydrogel over 24 h and the variation of ambient relative humidity.

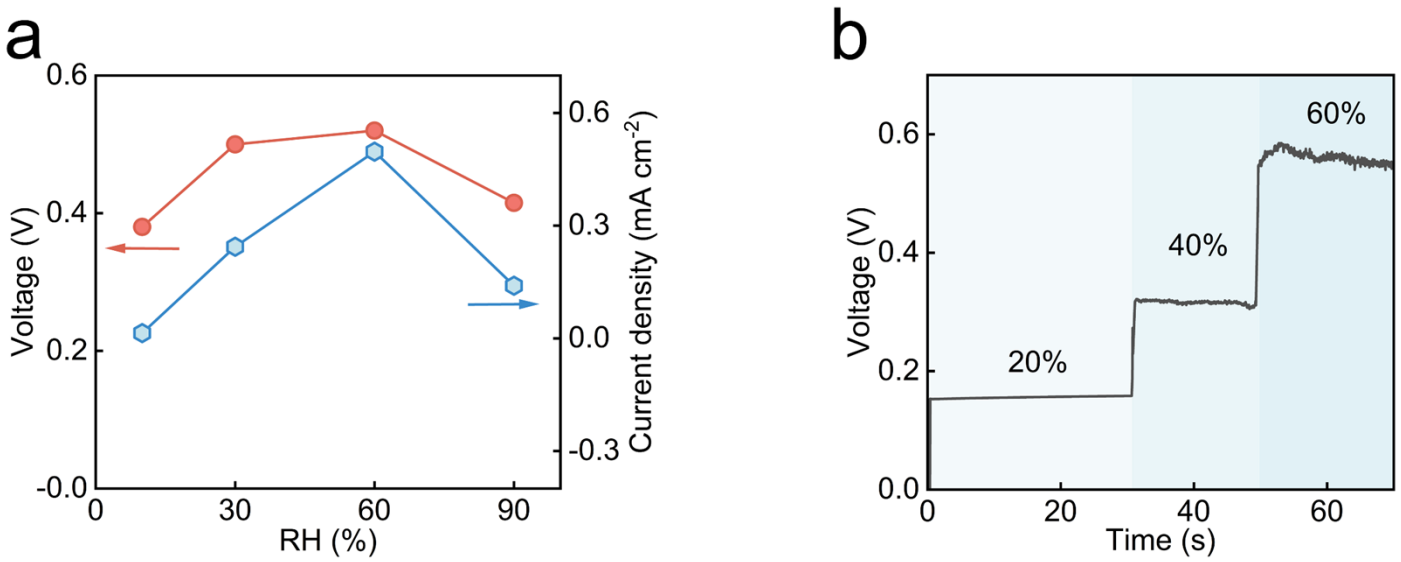


**Fig.S18** (a) Voc and $I_{SC}$ outputs of the MEG under varying relative humidity at 26 °C. (b) Voltage output of the MEG during continuous changes in humidity at 26 °C.

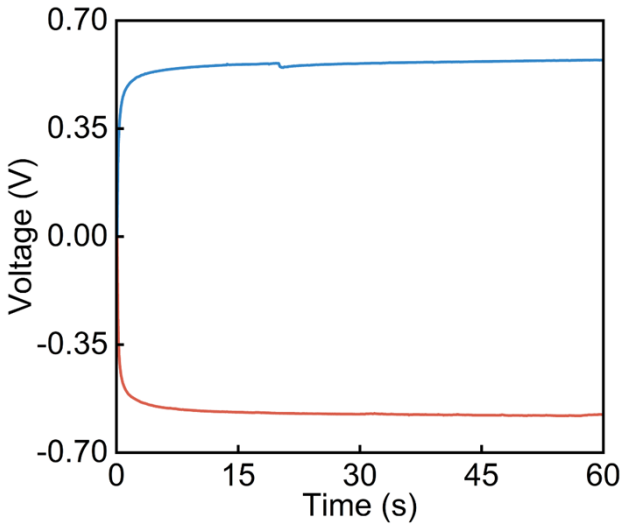


**Fig.S19** Voltage output of the MEG with interchanged electrodes.

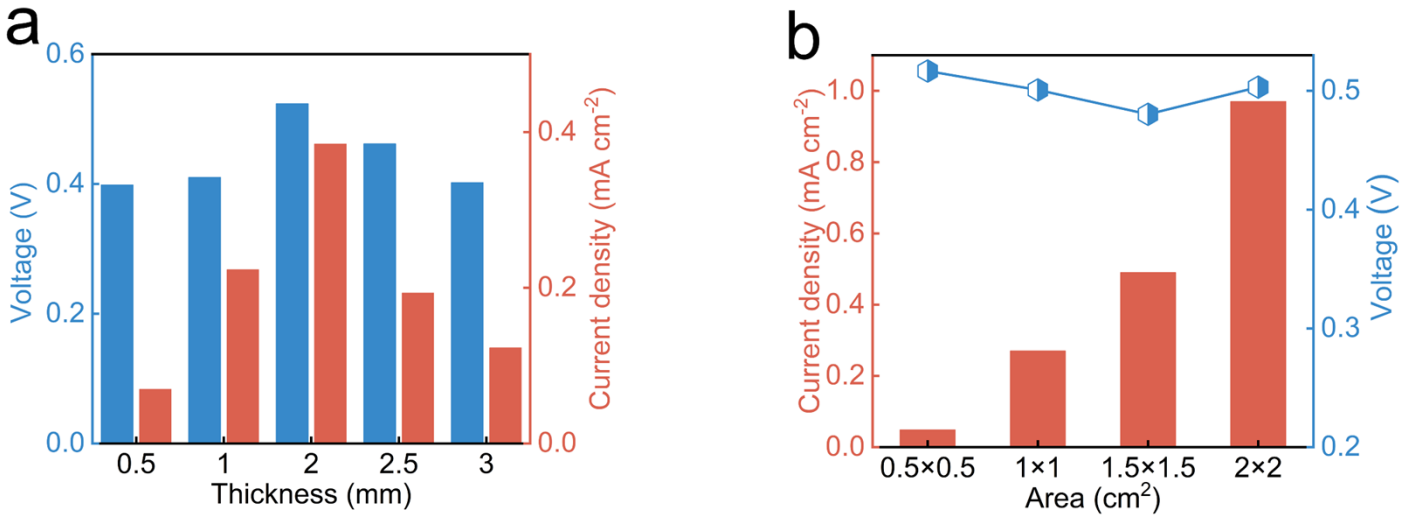


**Fig. S20** Voc and $I_{SC}$ outputs of the MEG. (a) MEG devices with active layers of different thicknesses. (b) MEG devices with different active areas.

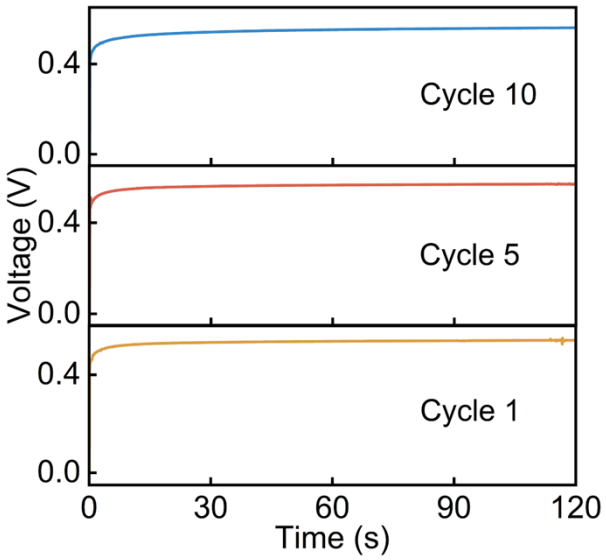


**Fig. S21** Cycling stability of the Voc output of the same MEG device over multiple cycles.

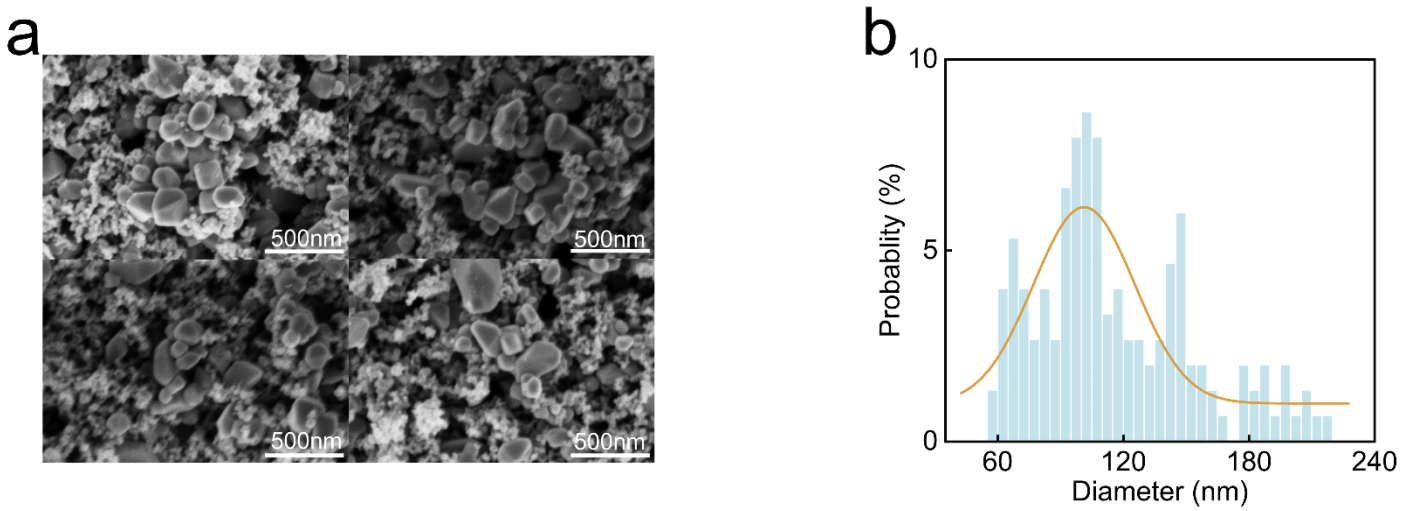


**Fig. S22** $TiO_2$ particle size distribution of (a) SEM image and (b) statistical analysis.

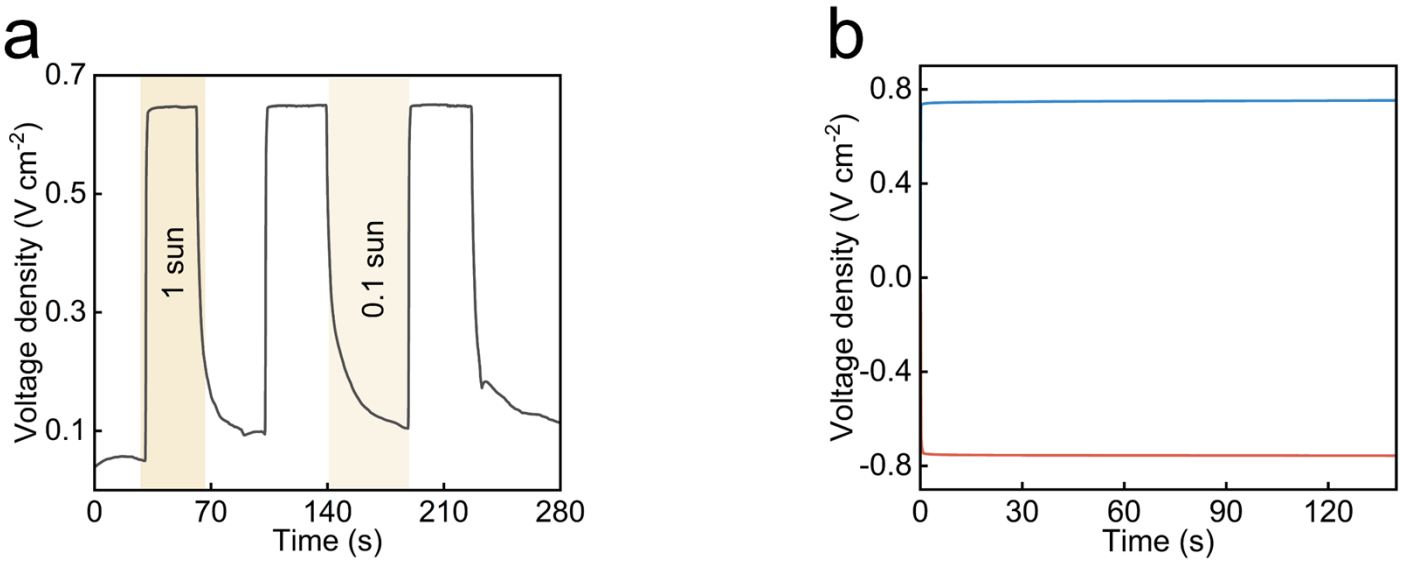


**Fig.S23** (a) Voc output of the solar energy side under different illumination conditions. (b) Voltage output of the SC with interchanged electrodes.

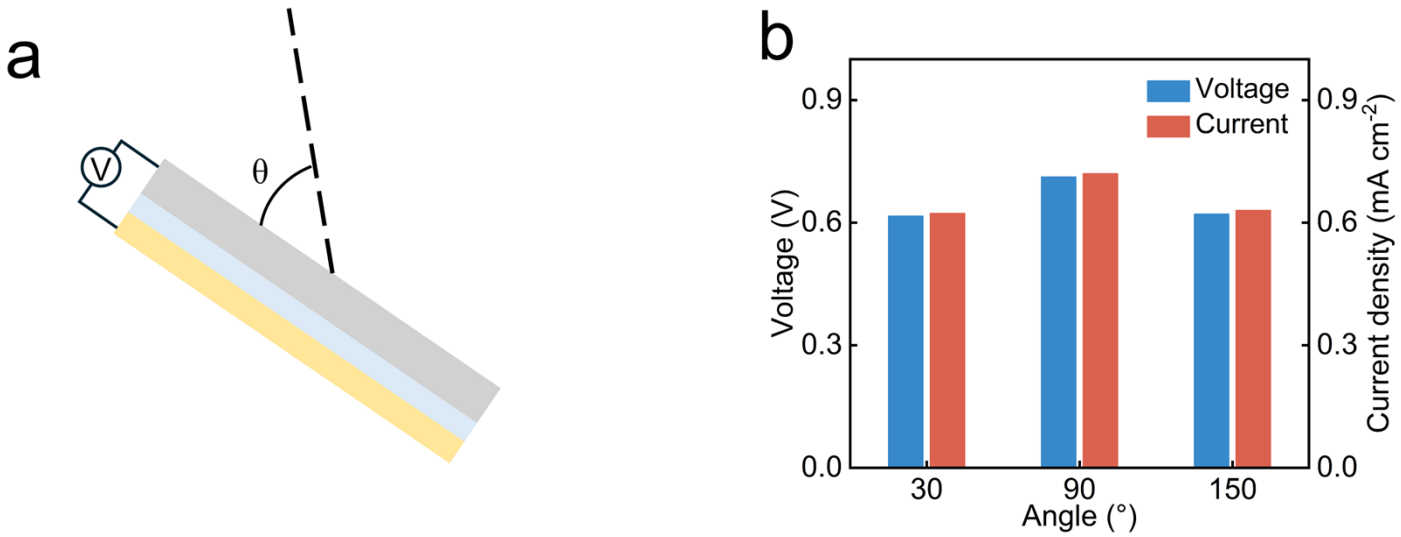


**Fig. S24** Effect of illumination angle on the electrical performance of the solar side under illumination of 100 mW $cm^{-2}$. (a) Schematic illustration of the illumination-angle configuration. (b) Voc and Isc outputs under different illumination angles.

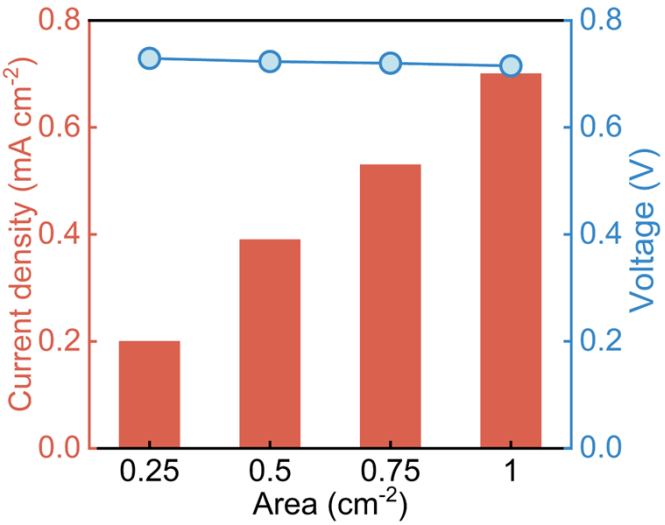


**Fig. S25** Voc and $I_{SC}$ of the solar side with different active areas under illumination of 100 mW $cm^{-2}$.

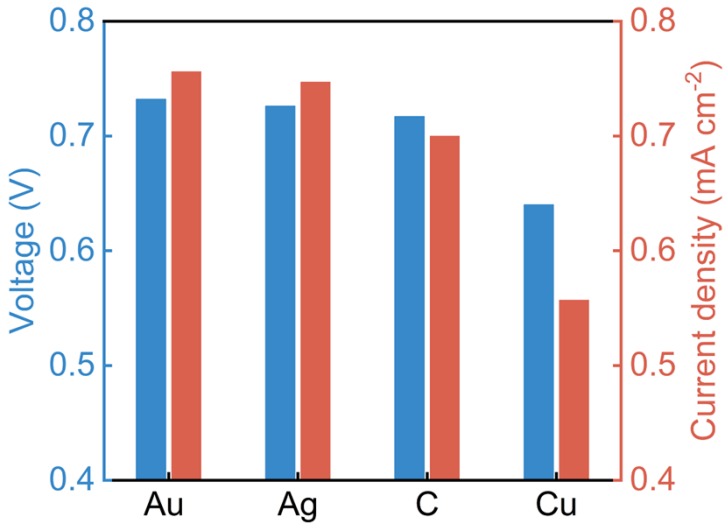


**Fig. S26** Electrical output of the SC with different electrode types under illumination of 100 mW $cm^{-2}$.

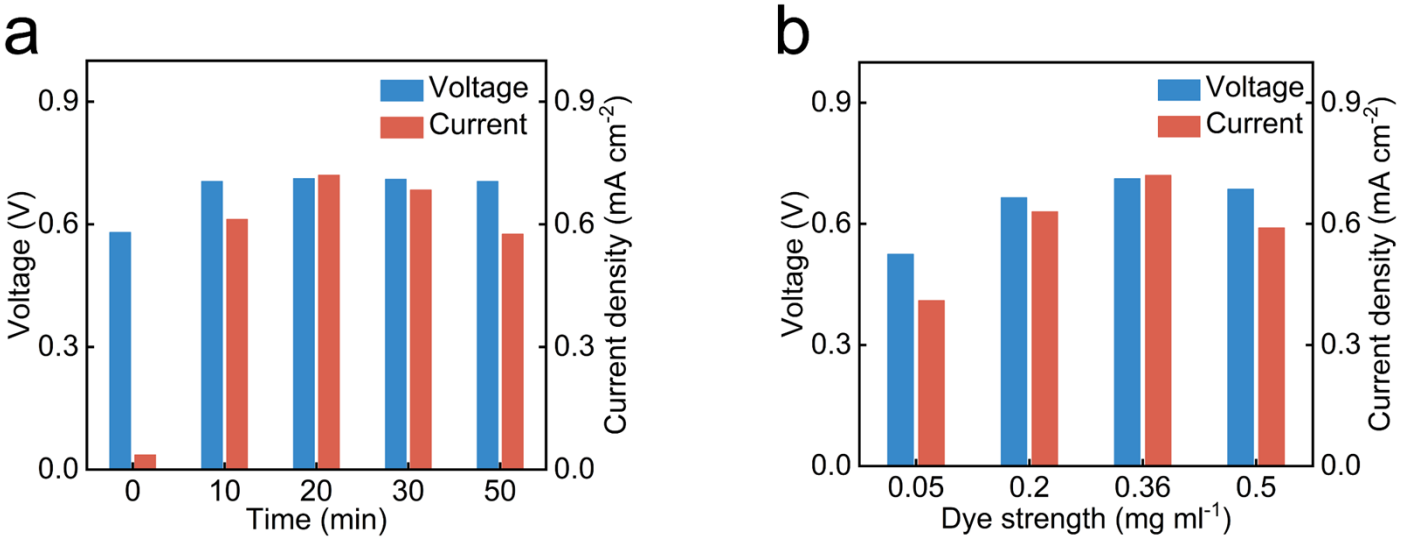


**Fig. S27** Effect of dye on the electrical performance of the SC under illumination of 100 mW $cm^{-2}$. (a) Influence of dyeing time. (b) Influence of dye concentration.

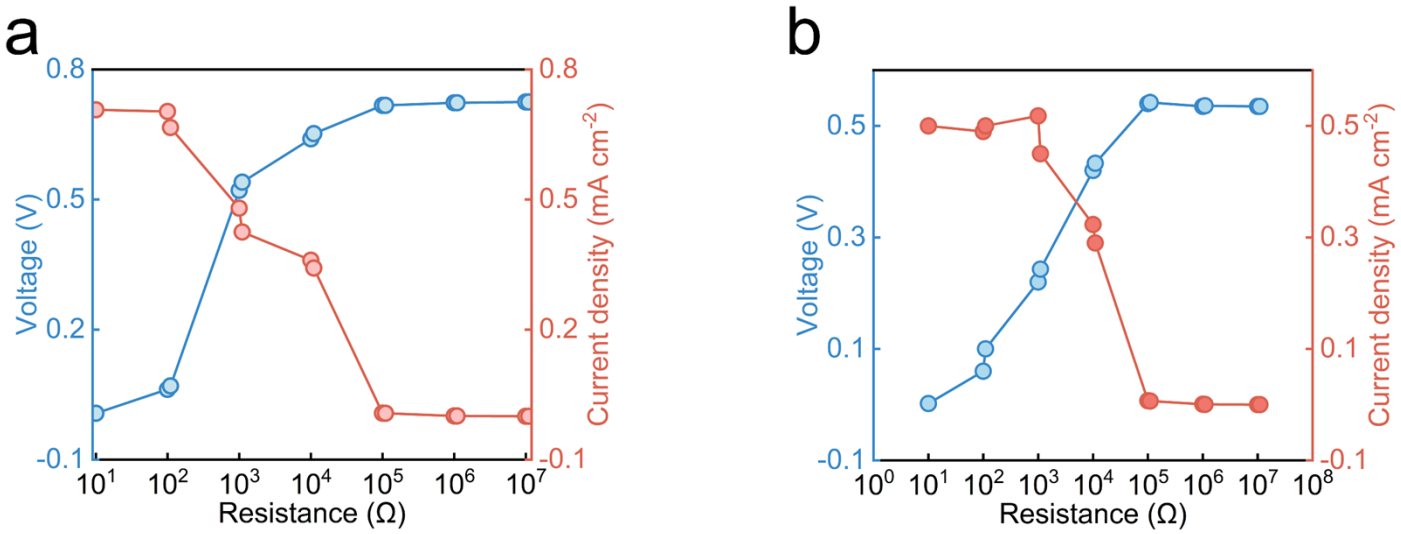


**Fig. S28** Voc and $I_{SC}$ outputs of the hybrid generator with external load resistances under illumination of 100 mW $cm^{-2}$ and RH of 60%. (a) SC side. (b) MEG side.

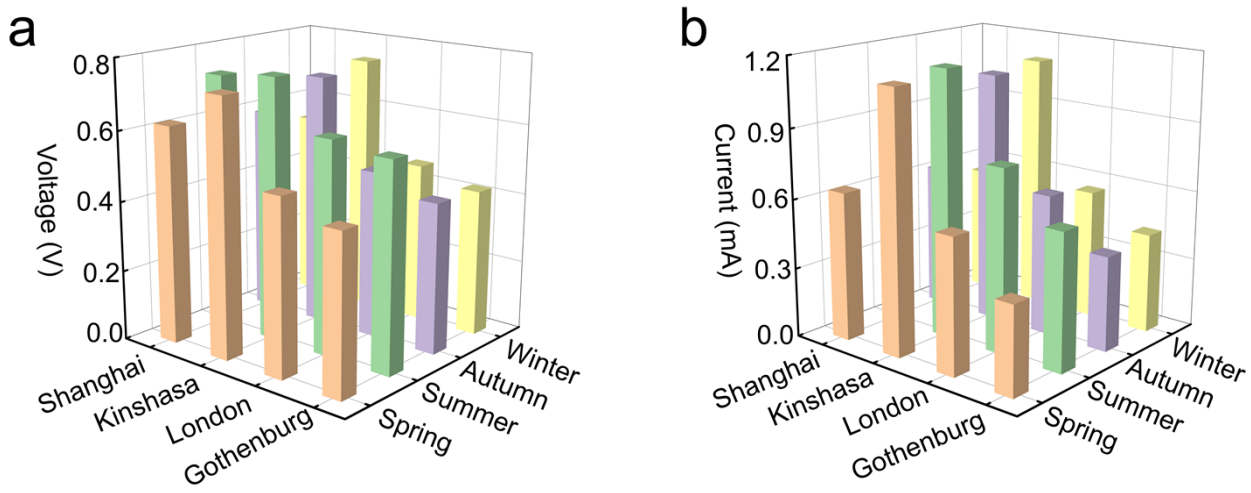


**Fig. S29** Electrical output of the MEG–SC hybrid generator in Shanghai, Kinshasa, London, and Gothenburg across four seasons: (a) voltage and (b) current. (Source: WorldClim official database)

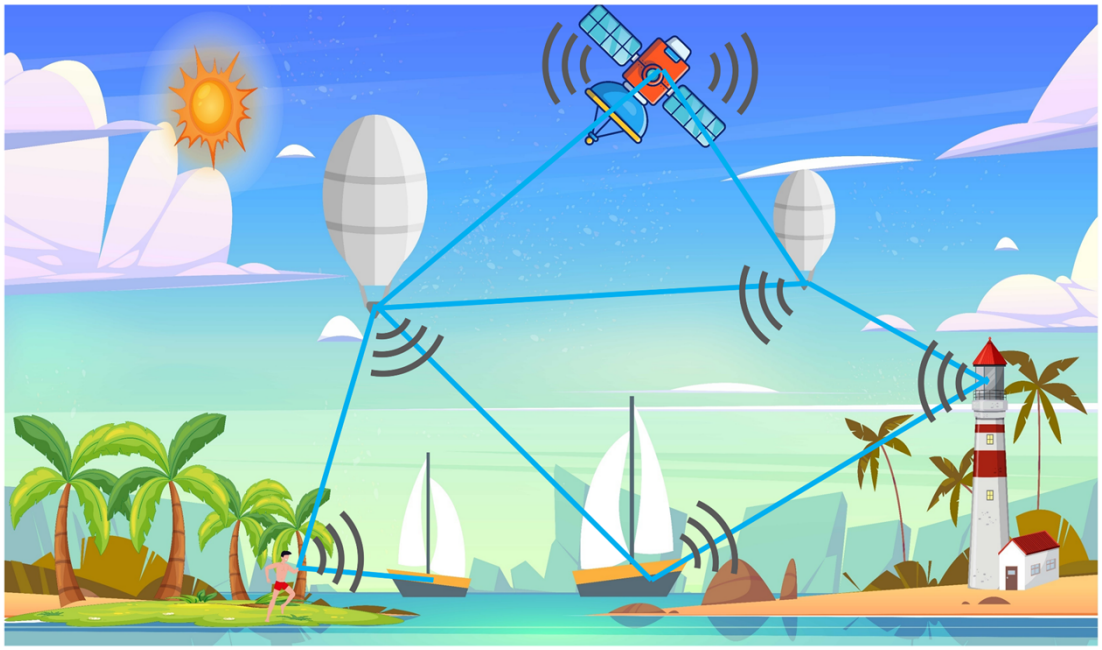

**Fig. S30** Demonstration of application scenarios for a wearable positioning and emergency alarm system.

| Sample | Groove depth / μm | Groove width / mm | Groove density / lines $cm^{-1}$ | ΔRH / % |
|---|---|---|---|---|
| FCE | | | | 5.3 |
| LCE-1 | 200 | 1 | 1.5 | 23.2 |
| LCE-2 | 200 | 0.5 | 1.5 | 17.6 |
| LCE-3 | 200 | 2 | 1.5 | 10.5 |
| LCE-4 | 100 | 1 | 1.5 | 12.3 |
| LCE-5 | 300 | 1 | 1.5 | 19.2 |
| LCE-6 | 200 | 1 | 1 | 12.0 |
| LCE-7 | 200 | 1 | 2 | 20.3 |

**FCE:** flat carbon electrode

**LCE:** laser-patterned carbon electrode

**Table S1** Optimization of laser-patterning parameters of carbon electrodes and their effects on humidity-gradient maintenance.

| Sample | Photothermal conversion efficiency / % | Contact area change / % | EIS response |
|---|---|---|---|
| Without microstructures | 17.6 | —— | Similar semicircle diameter |
| With microstructures | 16.6 | -27.8 | Similar semicircle diameter |

**Note:** All carbon paper samples used for laser-patterning optimization had a size of 2 cm × 2 cm and a thickness of approximately 1 mm. The laser-patterned traces were designed as grid-like grooves with a groove depth of 200 μm, a groove width of 1 mm, and a groove density of 1.5 lines $cm^{-1}$.

**Table S2** Comparison of photothermal conversion efficiency, electrode–hydrogel contact area change, and EIS response of the hybrid MEG–SC devices with and without laser-patterned microstructures.